

In-plane prestressing: Inspiration from a hair clip

Zechen Xiong¹, Liqi Chen², Wenxiong Hao², Pengfei Yang³, Xi Chen^{1,*}

¹*Department of Earth and Environmental Engineering, Columbia University, New York, NY 10027, USA*

²*Department of Mechanical Engineering, Columbia University, New York, NY 10027, USA*

³*School of Mechanical Engineering and Automation, Fuzhou University, Fuzhou 350108, China*

*Correspondence: *xichen863@hotmail.com*

Abstract

Structural instability is a hazard that leads to catastrophic failure and is generally avoided through special designs. A trend, however, has emerged over the past decades pointing to the harnessing of mechanisms with instability. Inspired by the snapping of a hair clip, we are finessing the unique characteristics of the lateral-torsional buckling of beams and the snap-through of pre-buckled dome-like thin-wall structures in a new field: the in-plane prestressed mechanism. Analyses reveal how the 2D-3D assembly of an in-plane prestressed actuator (IPA) is achieved and how the post-buckling energy landscape is pictured. Combining them with soft robotics, we show that the inclusion of a bistable IPA can enormously enhance the performance of an underwater fish robot as well as inspire a finger-like soft gripper.

Summary: new mechanism that offers a “free lunch” for soft robotics

Main Text

Multi-stable structures are recently found to be very useful in various smart materials, engineered structures, and novel applications spanning several orders of magnitude (1). Enlightened by an increasing understanding of buckling and post-buckling responses (2–4), in this study, we examine the idea of an in-plane prestressed mechanism that provides a new perspective for moving and transforming applications. Unlike the mechanical and economical benefits prestressing offers in civil engineering, the combination of instability and prestressing endows mechanisms with unprecedented functional mobility. Examples are not uncommon in nature. Many plants have “learned” to build up prestressed elastic energy through osmosis and turgor pressure. A sudden release of this energy can cause rapid movements and plays a critical role in their functions like reproduction and nutrition: the ballistic seed dispersal of Impatiens and squirting cucumber after prestressing their seedpods (5); the pollen dispersal of trigger plants (6); the rapid leaf closure of Venus flytrap (7), etc. Interestingly, this prestress-and-buckle mechanism is comparatively rare in the animal kingdom, possibly since it is often accompanied by structural fracture or eversion that animals cannot bear, although birds’ zero-powered perching (8) (prestressing) and the hummingbirds’ beak (9) (buckling) can be close exceptions. Prestressed structures seem to be an ideal option for morphing or robotic mechanisms.

Compared to traditional rigid robotics, soft prestressed mechanisms possess some advantages same as other soft structures do (10), including biocompatibility, versatility, and

economic viability, but further offer enhanced performance in force exertion, fast locomotion, and delicate manipulation. Especially, Tang et al. (11) proposed to use a prestressed hybrid structure composed of plastics, metallic spring, and pneumatic elastomers to rapidly locomote robots; Sun et al. (12) further demonstrated thermal pre-straining to fine-tune the energy landscape of a similar bistable jumping mechanism; Kim et al. and Huang et al. (13, 14) use respectively thermal- and mechanical-induced pre-strained mismatched composite laminates to create rapid deforming actuators. However, these mechanisms are complex in structure, assembly, and fabrication, which significantly compromises their practical use. To address this challenge and open a new way, we show in this work the method of implementing 2D-3D assembly of an in-plane prestressed bistable mechanism and its application potential.

The geometry and assembly of the in-plane prestressed actuator (IPA), shown in Fig. 1, are inspired by a single-piece metal hair clip that becomes bistable during manufacturing when its two extremities are pinned together. Please note that the term “actuator” in IPA, instead of describing a physical actuator like the shape memory alloy actuator, points to the motion-outputting feature of the structure. In a similar prestressing process illustrated in Fig. 1A, the lateral-torsional buckling of the props (denoted by L_2) of the “V” shape ribbon creates a thin-wall spatial surface with non-zero Gaussian curvatures, i.e., a dome; the minimization of the total of in-plane and out-of-plane strain energy gives it symmetrical bi-states that can be switched between by overcoming an energy barrier. Using common planar material like PE/PETG shims, the laser-cut strip can be assembled into an IPA with enhanced rigidity for force exertion, as well as reversible snap-through buckling for fast movement. Intriguingly, the global snap-through of the IPA can be triggered by local actuation of the central segment (denoted by L_1), while the extruded long props can be used as end effectors. This local-global actuation is called “bend-propagating actuation” in the relevant literature (13). The snapping takes only several milliseconds and can be triggered by assorted energy sources. We hope this mechanism not only sheds light on future compliant robotics but also inspires research in domains like origami/kirigami structure (15, 16), deployable devices (17, 18), and morphing airfoils (19, 20).

To characterize this mechanism, we build a mathematical model for its assembly and actuation, starting from the “V” shape ribbon with arbitrary parameters, as in Fig. 1A. After pinning the ends of the props together, the 2D ribbon becomes a spatial dome (Fig. 1B and 1C) and is locked into a higher energy state. According to the Gauss’ Theorema Egregium, this structure has zero degrees of freedom (DOF) and therefore should not be transformable; however, the pin connection between the ends loosens the rotational constraints, making achievable the ribbon’s bending deformation and thus the global snapping. This additional hidden DOF is separated from the rotational DOF of the ribbon by an energy gap that gives rise to a geometric bifurcation between the bi-states. This can be interesting when used in applications such as mechanical switches and actuators.

A detailed derivation of the model in Fig. 1D-1F is provided in the Supplementary Information (SI). Based on geometric approximation and energy conservation, the tip bending angle of an arbitrary IPA is found as

$$\psi_l \approx \frac{du}{dz} = -\frac{P_{cr}}{EI_\eta} \int_0^l \varphi(l-z) dz \quad (1)$$

in which EI_i is the bending stiffness of the corresponding axis, $l = L_1 + L_2$ is the half-length of the strip, and P_{cr} is the critical load of the lateral-torsional buckling, which is analytically given in the SI. Interestingly, the solution indicates that angle ψ_l , a key factor for the kinematic performance of IPA, is independent of the material modulus E and absolute dimensions like L_1 , L_2 , h , and t , yet is only affected by the unitless shape factors θ and γ_s (Fig. 1), if only the conditions are met that $h > 10t$ and the Poisson's ratio of the material is maintained. The comparison between theory and experiments gives an error within 5%, as shown in Fig. 2A and 2B.

Assuming the snapping of an IPA is similar to that of an axially pre-buckled beam with clamped ends (4), shown in Fig. 2D, the dimensionless energy barrier defined as $\bar{U}_{barr} = U_{barr} L_1 / EI_\eta$ can be approximated to be $\bar{U}_{barr} = \bar{U}_{max} - \bar{U}_{ini} = 3\bar{U}_{ini}$, in which \bar{U}_{max} and \bar{U}_{ini} are the strain energy of the IPA at bifurcation point and pre-buckled state (Fig. 1F), respectively. Movie S1 shows the snapping of a pneumatically actuated IPA (2I) with FE simulation, which gives a maximum error of ca. 10% compared to the theoretic solutions (Fig. 2E). Surprisingly, the scale-free nature of IPA is also observed in the energy analysis, since the energy gap \bar{U}_{barr} also depends merely on the parameters θ and γ_s , indicating total scalability in deformation and energy landscape. For example, increasing the thickness t by twofold yields unchanged ψ_l and \bar{U}_{barr} , while giving an eight-fold rise in U_{barr} . These features can inspire novel designs of morphing structures, metamaterial, and MEMS of both macro- and milli-scales, which are our future projects.

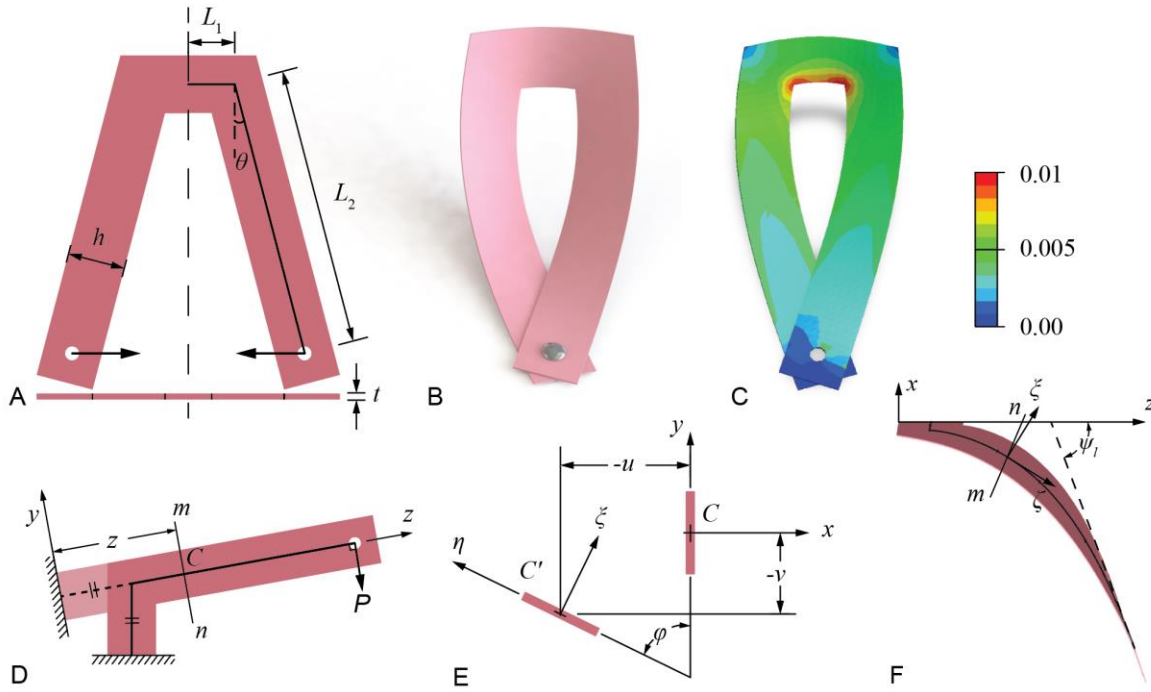


Fig. 1 **Design and mathematic model of a hair clip-inspired in-plane prestressed actuator (IPA).** (A) The geometry of the ribbon before assembly. (B) and (C) Assembled configuration and corresponding contour of maximum principal strain, respectively. Shape factors $\theta = 10^\circ$ and $\gamma_s = L_2/L_1 = 6$; other parameters $h/L_1 = 15\text{mm}/12.5\text{mm}$ and $t/L_1 = 0.381\text{mm}/12.5\text{mm}$. (D) The "straightened" equivalent model for theoretic analysis. (E) The displacements of the section mn and (F) the pre-buckled configuration of the structure.

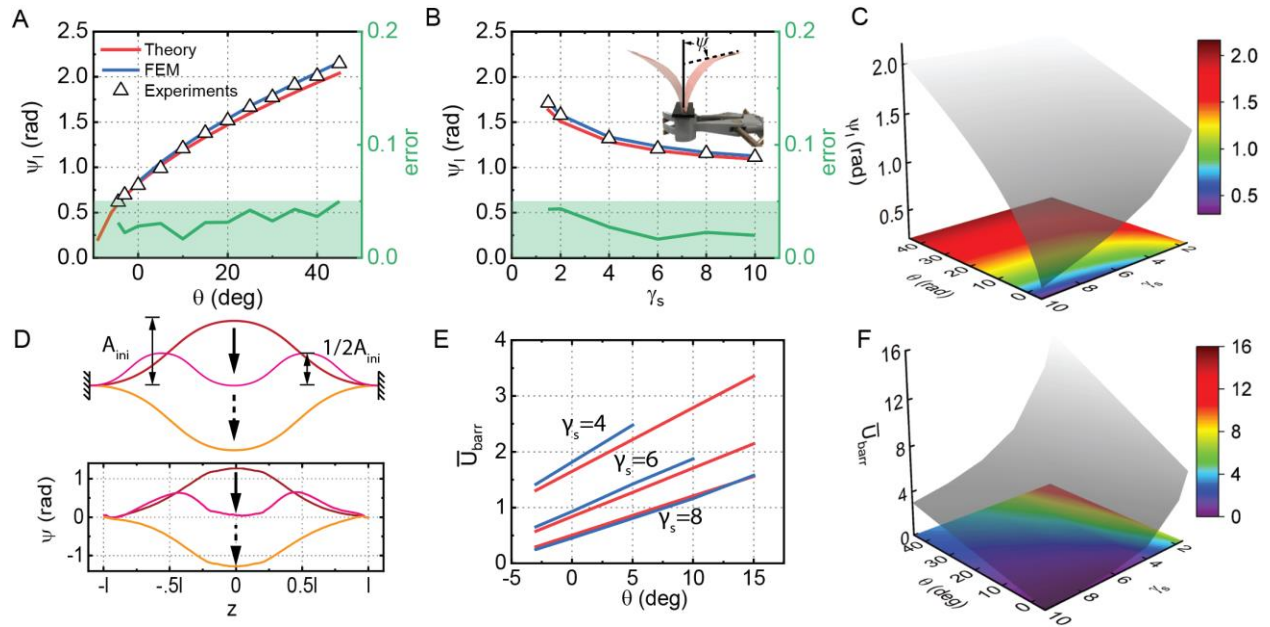


Fig. 2 **Characterization of the pre-buckling and the post-buckling of IPAs.** (A) and (B) Comparison of the value ψ_1 among theoretic model, FE reproduction, and experiment results w.r.t. varying prop angle θ and dimensionless prop

length γ_s , respectively. The region within 5% error (calculated by comparing the theory to experiments) is highlighted in green. Inset shows the bi-states and tip bending angle ψ_l . **(C)** and **(F)** Maps illustrating the designing spaces of θ and γ_s , respectively, w.r.t. ψ_l and the unitless energy gap \bar{U}_{barr} . **(D)** Comparison of snap-through evolutions between the theory and the FE reproduction. A_{ini} denotes the deflection “amplitude” of a pre-buckled curve. **(E)** Comparison between theory and FE results of \bar{U}_{barr} w.r.t. shape factors θ and γ_s .

Inspired by the undulating motion of the compliant body in fishes, we decide to assemble an IPA into a pneumatic fish robot to demonstrate its function. The structure of an easy-fabricated and -assembled fish robot is illustrated in Fig. 3A. It composes of two parts: a pneumatic-driven IPA (film thickness $t_1=0.381\text{mm}$) with a riveted thinner plastic sheet as the caudal fin (film thickness $t_2=0.191\text{mm}$) to enhance the propelling force, and a hollow 3D-printed fish head to guide and balance the motion as well as to encapsulate any future control and energy systems. It is found that an IPA with prop angles $\theta = -3^\circ$ is sufficient to drive the soft robotic fish at high speed. With an actuating pressure of 150kPa and a frequency of 1.3Hz (period=760ms), the IPA-based bistable pneumatic soft robotic fish swims at an averaged underwater horizontal velocity of 26.54 cm/s (calculated from simple trigonometry), or 1.40 body length per second (BL/s), which is twice as fast as the monostable reference swimmer with the same actuation conditions (Fig. 3B and movie S2) and very close to the threshold of swimming capacity of biological fishes (2 to 10BL/s (22)). This difference can be identified clearer in Fig. 4 and movie S3, where the single strike distance of the IPA-driven fish robot matches that of a real fish (23), yet the reference model only halves. In Fig. 3C are depicted the kinematics of the two robots, measured from high-fps videos. A near-triangular actuation signal is featured in the reference swimmer, while the IPA-driven one shows nonlinear swinging that resembles real fish, gaining more kinetic energy in a series of short bursts of angular displacement of the caudal fin, thus is more efficient. Compared to all other state-of-the-art predecessors (11, 22, 24–26), our work not only excels in velocity (fig. S3) but also triumphs in light-weightedness and simplicity of fabrication and assembly. If needed, the IPA-driven swinging can be even stronger if we increase any of the actuation frequency and the configuring parameter θ , yet may require a higher working pressure (movie S4, 2.5Hz, $\theta=10^\circ$, ~300kPa) which lowers the efficiency due to larger loss in the pneumatic system. The amazing function of IPA can help soft robots chase biomimetic locomotion speed.

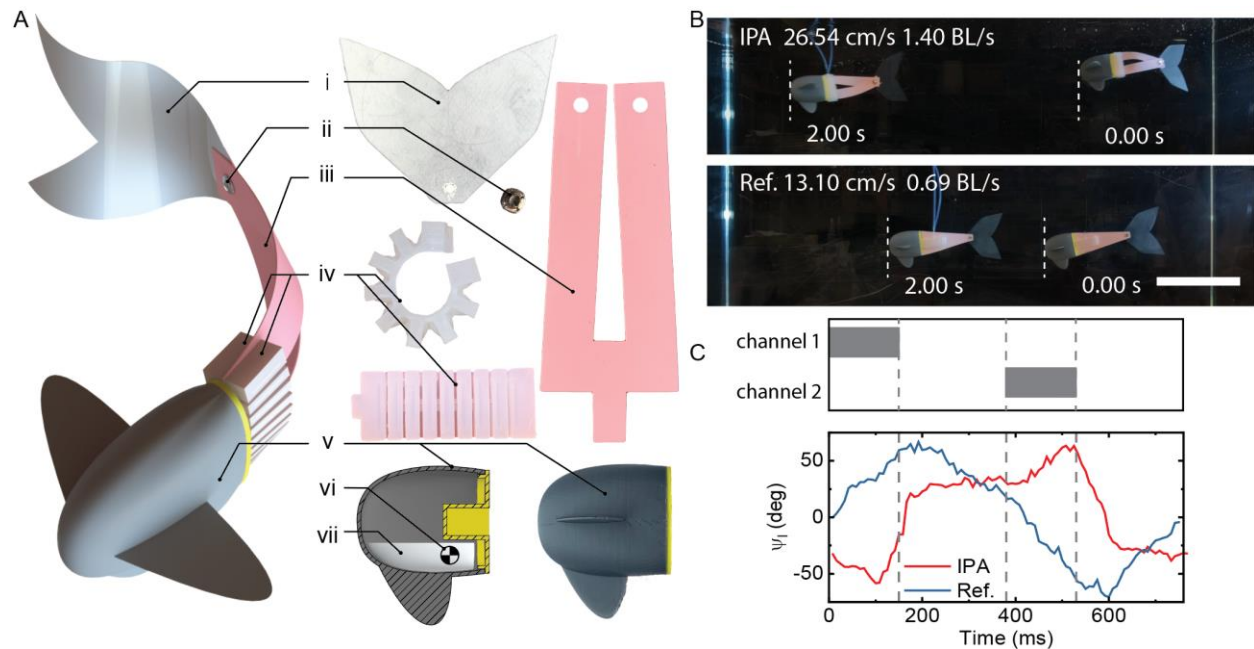


Fig. 3 IPA-driven fish robot and comparisons. (A) Assembly schematics of the robotic fish. i. caudal fin ($t=0.191\text{mm}$), ii. rivet pin, iii. IPA plate ($t=0.381\text{mm}$, $\theta=-3^\circ$, and $\gamma_s=6$), iv. antagonistic pair of pneumatic bending units (fabrication and dimension details shown in methods and fig. S1), v. 3D-printed hollow fish head, vi. location of the mass center after assembly, and vii. casted ballast. (B) Comparison of underwater locomotion between IPA-driven bistable fish robot and its monostable counterpart. Velocities are calculated from simple trigonometry. Scale bar, 150mm. (C) Comparison between the angular displacement ψ_i patterns of the two prototypes under 150kPa and 1.3Hz pressurization (period=760ms). Grey areas show when a channel is pressurized.

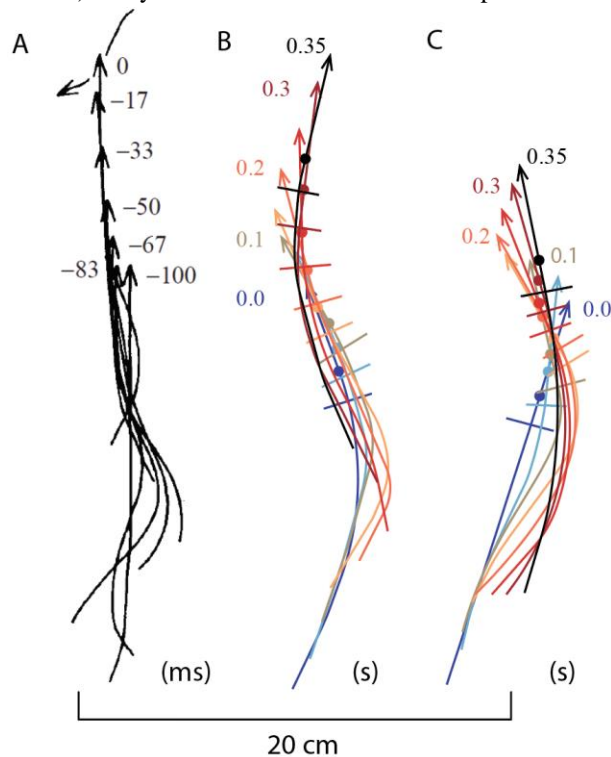


Fig. 4 **Comparison of strike patterns and sequences between biological and robotic fish.** (A) Strike pattern of a pike (*Esox* sp.) when hunting a smaller fish. Times are measured backward and in milliseconds. Reproduced from Webb and Skadsen (27). (B) and (C) Swimming sequences of body midlines and centers of mass (filled circles) in a single strike of the IPA-driven and the referential soft robotic fish, respectively. Short bars are the connection between fish heads and tails. Times are measured forward and in seconds.

To further demonstrate the versatility of IPA, we build a bistable soft gripper, as in Fig. 5. Being simple in structure, this IPA gripper can do human-like “pinching” grasps that pick up a piece of initially-flat soft fabric (Fig. 5A and 5B), which is rarely achieved even in rigid manipulators (28). This is because the IPA gripper features a human nail-like geometry that can deal with tiny and deformable objects, while the lack of compliance in rigid grippers and the bulkiness of full-elastomer bodies in classic soft manipulators render them inappropriate for this task. Researchers are utilizing similar theories to enhance grasping precision, reliability, and dexterity (29, 30), and the in-plane prestressed mechanism in this work expands the spectrum. Besides, the IPA bistable gripper has a payload several times its self-weight (Fig. 5C) and only consumes energy when a transition between relaxed mode and actuated mode is needed, due to its bistable nature. We hope this study can improve the performance of assorted compliant mechanisms and initiate a revolution in structural designs of soft robotics.

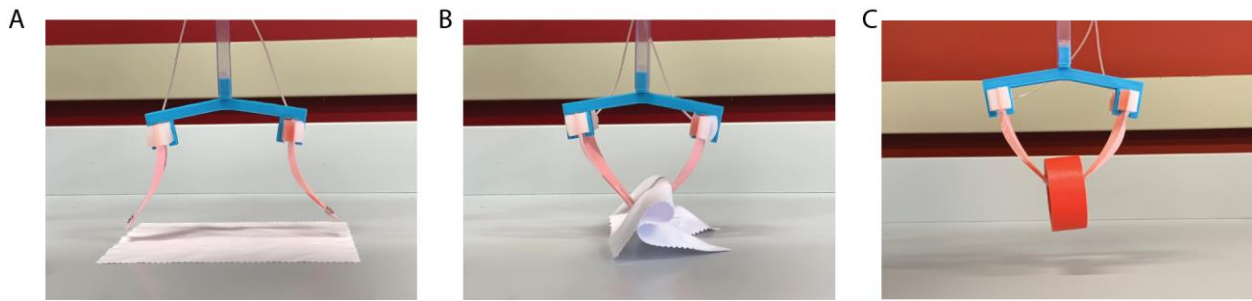


Fig. 5 **IPA-driven bistable soft gripper.** (A) and (B) Grasp of a thin and soft cloth. (B) Grasp of a roll of tape (44g, total weight of the gripper: 15g, factor $\theta=0^\circ$).

Harnessing the prestressing and instable modifications of 2D materials opens the way to smart structures with enhanced capability and functionality, inspiring applications in diverse fields and scales. Without compromising the structural unity and cost competitiveness, in-plane prestressed instability can be a “free lunch” that achieves better performance for next-generation metamaterials, morphing structures, and soft robotics.

References and Notes

1. N. Hu, R. Burgueño, Buckling-induced smart applications: recent advances and trends. *Smart Mater. Struct.* **24**, 063001 (2015).
2. S. P. Timoshenko, J. M. Gere, *Theory of Elastic Stability* (Courier Corporation, 2009).
3. L. L. Howell, in *21st Century Kinematics*, J. M. McCarthy, Ed. (Springer London, London, 2013; http://link.springer.com/10.1007/978-1-4471-4510-3_7), pp. 189–216.
4. Y. Zhang, Y. Jiao, J. Wu, Y. Ma, X. Feng, Configurations evolution of a buckled ribbon in response to out-of-plane loading. *Extreme Mechanics Letters.* **34**, 100604 (2020).
5. R. D. Deegan, Finessing the fracture energy barrier in ballistic seed dispersal. *PNAS.* **109**, 5166–5169 (2012).
6. P. E. Taylor, G. Card, J. House, M. H. Dickinson, R. C. Flagan, High-speed pollen release in the white mulberry tree, *Morus alba* L. *Sex Plant Reprod.* **19**, 19–24 (2006).
7. Y. Forterre, J. M. Skotheim, J. Dumais, L. Mahadevan, How the Venus flytrap snaps. *Nature.* **433**, 421–425 (2005).
8. A. Pal, D. Goswami, R. V. Martinez, Elastic Energy Storage Enables Rapid and Programmable Actuation in Soft Machines. *Advanced Functional Materials.* **30**, 1906603 (2020).
9. M. L. Smith, G. M. Yanega, A. Ruina, Elastic instability model of rapid beak closure in hummingbirds. *Journal of Theoretical Biology.* **282**, 41–51 (2011).
10. F. Ilievski, A. D. Mazzeo, R. F. Shepherd, X. Chen, G. M. Whitesides, Soft Robotics for Chemists. *Angewandte Chemie International Edition.* **50**, 1890–1895 (2011).
11. Y. Tang, Y. Chi, J. Sun, T.-H. Huang, O. H. Maghsoudi, A. Spence, J. Zhao, H. Su, J. Yin, Leveraging elastic instabilities for amplified performance: Spine-inspired high-speed and high-force soft robots. *Sci. Adv.* **6**, eaaz6912 (2020).
12. J. Sun, B. Tighe, J. Zhao, in *2020 IEEE International Conference on Robotics and Automation (ICRA)* (2020), pp. 10082–10088.
13. S.-W. Kim, J.-S. Koh, J.-G. Lee, J. Ryu, M. Cho, K.-J. Cho, Flytrap-inspired robot using structurally integrated actuation based on bistability and a developable surface. *Bioinspir. Biomim.* **9**, 036004 (2014).
14. X. Huang, K. Kumar, M. K. Jawed, A. M. Nasab, Z. Ye, W. Shan, C. Majidi, Chasing biomimetic locomotion speeds: Creating untethered soft robots with shape memory alloy actuators. *Science Robotics.* **3** (2018), doi:10.1126/scirobotics.aau7557.

15. Y. Yang, K. Vella, D. P. Holmes, Grasping with kirigami shells. *Science Robotics*. **6**, eabd6426 (2021).
16. Y. Tang, G. Lin, S. Yang, Y. K. Yi, R. D. Kamien, J. Yin, Programmable Kiri-Kirigami Metamaterials. *Advanced Materials*. **29**, 1604262 (2017).
17. Z. Xiong, H. Xiao, X. Chen, Fractal-inspired soft deployable structure: a theoretical study. *Soft Matter*. **17**, 4834–4841 (2021).
18. W. Wang, H. Rodrigue, S.-H. Ahn, Deployable Soft Composite Structures. *Scientific Reports*. **6**, 20869 (2016).
19. S. Daynes, K. D. Potter, P. M. Weaver, Bistable prestressed buckled laminates. *Composites Science and Technology*. **68**, 3431–3437 (2008).
20. S. Daynes, P. M. Weaver, Stiffness tailoring using prestress in adaptive composite structures. *Composite Structures*. **106**, 282–287 (2013).
21. B. Mosadegh, P. Polygerinos, C. Keplinger, S. Wennstedt, R. F. Shepherd, U. Gupta, J. Shim, K. Bertoldi, C. J. Walsh, G. M. Whitesides, Pneumatic Networks for Soft Robotics that Actuate Rapidly. *Advanced Functional Materials*. **24**, 2163–2170 (2014).
22. R. K. Katzschmann, J. DelPreto, R. MacCurdy, D. Rus, Exploration of underwater life with an acoustically controlled soft robotic fish. *Science Robotics*. **3** (2018), doi:10.1126/scirobotics.aar3449.
23. P. Domenici, R. Blake, The kinematics and performance of fish fast-start swimming. *Journal of Experimental Biology*. **200**, 1165–1178 (1997).
24. A. D. Marchese, C. D. Onal, D. Rus, Autonomous Soft Robotic Fish Capable of Escape Maneuvers Using Fluidic Elastomer Actuators. *Soft Robotics*. **1**, 75–87 (2014).
25. Airacuda | Festo USA, (available at https://www.festo.com/us/en/e/about-festo/research-and-development/bionic-learning-network/highlights-from-2006-to-2009/airacuda-id_33879/).
26. T. Li, G. Li, Y. Liang, T. Cheng, J. Dai, X. Yang, B. Liu, Z. Zeng, Z. Huang, Y. Luo, T. Xie, W. Yang, Fast-moving soft electronic fish. *Science Advances*. **3**, e1602045 (2017).
27. P. W. Webb, J. M. Skadsen, Strike tactics of *Esox*. *Can. J. Zool.* **58**, 1462–1469 (1980).
28. J. Shintake, V. Cacucciolo, D. Floreano, H. Shea, Soft Robotic Grippers. *Advanced Materials*. **30**, 1707035 (2018).
29. L. U. Odhner, R. R. Ma, A. M. Dollar, in *2012 IEEE International Conference on Robotics and Automation* (2012), pp. 2830–2835.
30. J. Zhou, S. Chen, Z. Wang, A Soft-Robotic Gripper With Enhanced Object Adaptation and Grasping Reliability. *IEEE Robotics and Automation Letters*. **2**, 2287–2293 (2017).

31. H. Jin, E. Dong, G. Alici, S. Mao, X. Min, C. Liu, K. H. Low, J. Yang, A starfish robot based on soft and smart modular structure (SMS) actuated by SMA wires. *Bioinspir. Biomim.* **11**, 056012 (2016).
32. F. G. Serchi, A. Arienti, C. Laschi, Biomimetic Vortex Propulsion: Toward the New Paradigm of Soft Unmanned Underwater Vehicles. *IEEE/ASME Transactions on Mechatronics.* **18**, 484–493 (2013).
33. S.-H. Song, M.-S. Kim, H. Rodrigue, J.-Y. Lee, J.-E. Shim, M.-C. Kim, W.-S. Chu, S.-H. Ahn, Turtle mimetic soft robot with two swimming gaits. *Bioinspir Biomim.* **11**, 036010 (2016).
34. M. D. Bartlett, N. Kazem, M. J. Powell-Palm, X. Huang, W. Sun, J. A. Malen, C. Majidi, High thermal conductivity in soft elastomers with elongated liquid metal inclusions. *PNAS.* **114**, 2143–2148 (2017).

Acknowledgments

We especially thank Yichao Tang and Jiahao Wu for their help with the experiments, Jiefeng Sun for the simulation suggestion, and all colleagues for the inspiring discussions. **Funding:** This work was supported by the Earth Engineering Center and the Center for Advanced Materials for Energy and Environment at Columbia University. **Author contributions:** Z. X. conceived the presented idea, developed the theory, built the simulation, and wrote the manuscript. L. C., W. H., and P. Y. designed and carried out the experiments. X. C. supervised the project. **Competing interests:** There are no conflicts of interest to declare. **Data and materials availability:** All data are available in the manuscript or supplementary materials.

Supplementary Materials

Materials and Methods

fig. S1 to S3

Captions for movie S1 to S4

movies S1 to S4

Supplementary Materials for:
In-plane prestressing: Inspiration from a hair clip

The PDF file includes:

Materials and methods

fig. S1 to S3

Captions for movie S1 to S4

Other Supplementary Material:

movies S1 to S4

Materials and Methods

Finite element method

The finite element (FE) analyses of the configuration (Fig. 1B, Fig. 2A-C), maximum principal strain contour (Fig. 1C), and snap-through buckling (movie S1) of the prestressed in-plane prestressed actuator (IPA) is created using ABAQUS/CAE and solved with ABAQUS/Standard. All simulations use shell element S4R and the material is assumed to be linear elastic with a Young's modulus (E) of 2GPa and Poisson ratio (ν) of 0.3, if not specified.

Fabrication and measurement

The IPAs are laser-cut from the color-coded shims (McMaster-Carr, 9536K) and pin-locked by the press-fit rivets (McMaster-Carr, 97362A). The pneumatic soft bending units are fabricated using the 3D-printed molds (Ultimaker S3, PLA) and soft lithography reported in the literature (21) (fig. S1), with Dragon Skin 20 (Smooth-On Inc.) used and glued to the shims after curing using Loctite Super Glue (Plastics Bonding, 681925).

Bending angles of assembled IPAs are measured using 1-Axis Soft Flex Sensor (Bend Labs Inc.) and microcontroller of SparkFun Pro nRF52840 Mini (fig. S2).

Analytic solutions to the IPA

For the IPA ribbon in Fig. 1, total deflection of the section mn is depicted by the components u , v , and φ , which are the displacements of the centroid C in the directions of axes x , y , and z (Lagrangian coordinates), respectively, whose signs follow the directions of axes and right-hand rule. Meanwhile, the axes ξ , η , and ζ (Euler coordinates) are drawn through the deformed centroid C' , coinciding with the principal axes of the deformed configuration. Plugging in the classic Euler-Bernoulli and lateral-torsional buckling theories of beams (2), the deformation of the equivalent straight beam model in Fig. 1D can be characterized by the following equations:

$$EI_{\xi} \frac{d^2 v}{dz^2} + P(l - z) = 0 \quad (2)$$

$$EI_{\eta} \frac{d^2 u}{dz^2} + P\varphi(l - z) = 0 \quad (3)$$

$$T \frac{d\varphi}{dz} + P(l - z) \frac{du}{dz} - P(u_1 - u) = 0 \quad (4)$$

in which EI_i is the bending stiffness of i axis, $l = L_1 + L_2$ is the half-length of the strip, $T = GJ = hb^3G/3$ is the torsional rigidity of the thin rectangular section mn , u_1 the horizontal deflection at $z = l$, and G the shear modulus. Differentiating Eq. **Error! Reference source not found.** w.r.t z and plugging in Eq. (2) yield

$$T \frac{d^2 \varphi}{dz^2} + \frac{P^2 (l-z)^2}{EI_\eta} \varphi = 0 \quad (5)$$

The general solution of Eq. **Error! Reference source not found.** can be analytically given as

$$\varphi = \sqrt{s} \left[A_1 J_{1/4} \left(\frac{\beta_1}{2} s^2 \right) + A_2 J_{-1/4} \left(\frac{\beta_1}{2} s^2 \right) \right] \quad (6)$$

where $s = l - z$, $J_{1/4}$ and $J_{-1/4}$ represent Bessel functions of the first kind of order 1/4 and -1/4, respectively, notation

$$\beta_1 = \sqrt{\frac{P^2}{EI_\eta C}} \quad (7)$$

and due to the symmetry of the ribbon integration constant $A_2=0$ can be determined from the boundary conditions

$$\varphi|_{s=0} = 0 \quad (8)$$

and

$$\varphi = \sqrt{s} A_1 J_{1/4} \left(\frac{\beta_1}{2} s^2 \right) \quad (9)$$

which means the ribbon buckles approximately in the shape of a Bessel function. Similarly, from the riveting of the ends of the ribbon,

$$\varphi|_{s=l} = 0 \quad (10)$$

can be assumed. Due to the lack of lateral support on the beams, the lowest root of the Bessel function should be used, which yields

$$\frac{\beta_1}{2} l^2 = 2.7809 \quad (11)$$

and thus

$$P_{cr} = \frac{5.5618}{l^2} \cdot \sqrt{EI_\eta C} \quad (12)$$

To determine the value of constant A_1 , one additional equation, usually the energy conservation equation, is needed, which dictates that the total elastic strain energy of the structure must equal the work done by the external load. Ignoring the membrane strain energy, we have

$$U = \frac{1}{2} \int_0^l \left[P_{cr}^2 (l-z)^2 \sin^2 \varphi / EI_\eta + GJ (\varphi')^2 \right] dz \quad (13)$$

$$T = P_{cr} \cdot L_2 \left(\sin^{-1} \frac{1}{\gamma_s} + \theta \right) \quad (14)$$

in which U is the elastic strain energy of arbitrary A_1 , and T is the external work done by P_{cr} . From

$$U = T \quad (15)$$

the typical values of A_1 can be calculated as 0.09~0.10, depending on the value of γ_s and θ . Finally, by plugging Eq. **Error! Reference source not found.** into Eq. **Error! Reference source not found.**, the bending angle ψ of the section mn (Fig. 1) can be calculated from

$$\psi \approx \frac{du}{dz} = -\frac{P_{cr}}{EI_\eta} \int_0^z \varphi (l-z) dz \quad (16)$$

Of course, these solutions are only first-order approximations due to multiple assumptions used, yet still offer insights into the study and use of IPAs.

Figures

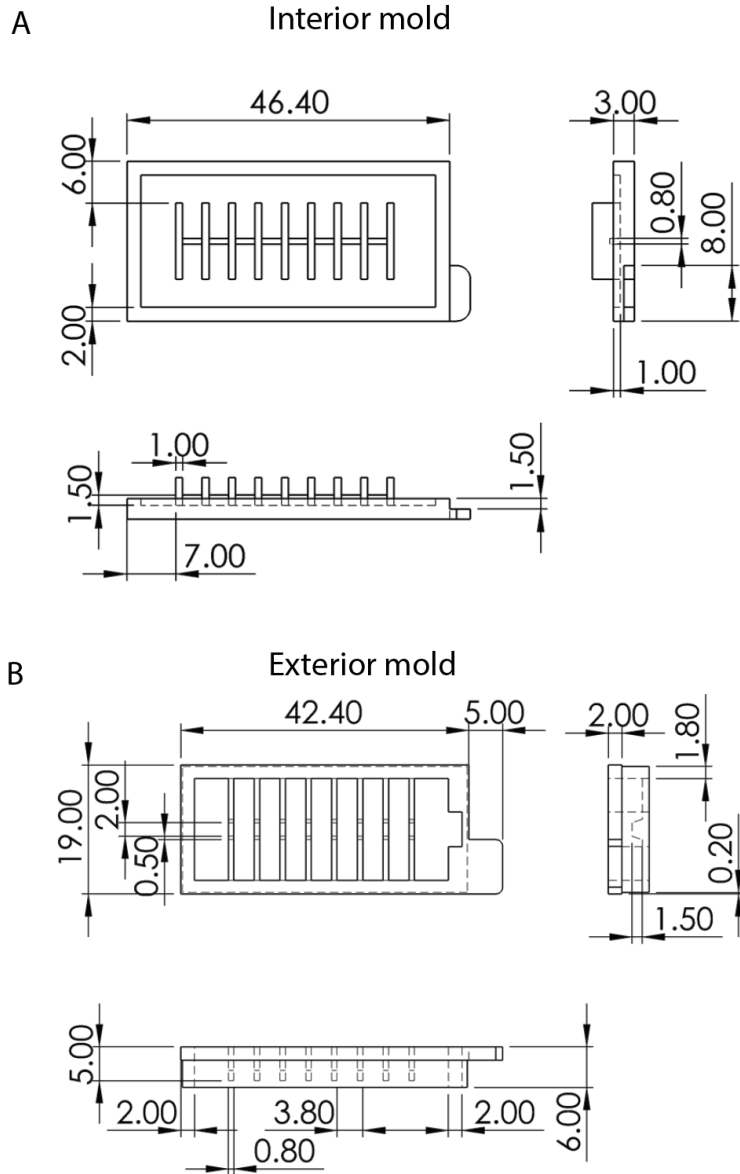


fig. S1 Molds for the fabrication of the antagonistic pneumatic bending pair. **(A)** Dimensions (mm) for the interior mold for the pneumatic bending unit. Shown are 2D drawings of the top, side, and front views. **(B)** Dimensions for the exterior mold for the pneumatic bending unit. Shown are 2D drawings of the top, side, and front views.

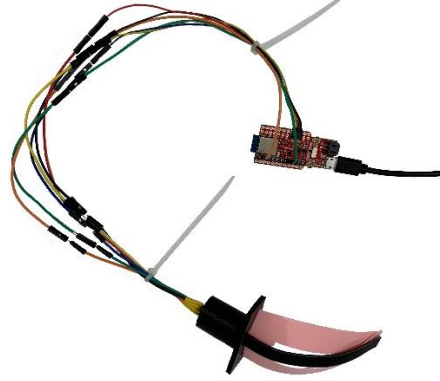


fig. S2 Experimental setup for the measurement of bending angles for the assembled IPA.

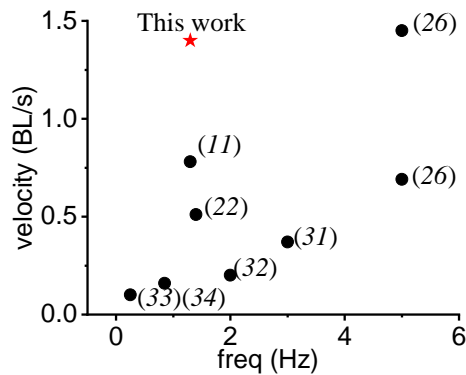


fig. S3 Comparison of swimming velocity w.r.t actuation frequency among the IPA-driven and various reported soft underwater robotic swimmers. The dots marked with “3” are surface cruising robots.

Movie captions:

movie S1. FE simulation on actuating the bistable pneumatic-powered IPA. The shape factor of the IPA ribbon: $\theta=10^\circ$, $\gamma_s=L_2/L_1=6$.

movie S2. The Comparison of real-time swimming of the IPA-driven fish robot and its conventional soft counterpart. The pneumatic actuation system pressurizes at 150kPa and 1.3Hz.

movie S3. The Comparison of slow-motion swimming of the IPA-driven fish robot and its conventional soft counterpart. The movie is filmed at 240 fps, in which the actuating pneumatic system offers a pulse of 150kPa and 1.3Hz.

movie S4. The high-frequency real-time swinging of the bistable IPA-driven soft robotic fishtail. The pneumatic actuation system pressurizes at ~ 300 kPa and 2.5Hz.